infrastructures

MDPI

Article

Deformation Characteristics of Narrow Coal Pillar Roadway Incorporating the Roof Cutting Technique

Changle Ma [1], Yuewen Pan [2,*], Feng Zhou [3] and Yafei Zhou [4,*]

[1] Gaojiazhuang Coal Mine, Shanxi Lu'an Mining (Group) Co., Ltd., Changzhi 046000, China; 15135557198@163.com
[2] Xuchen Mining Technology Development (Xuzhou) Co., Ltd., Xuzhou 221116, China
[3] Wangzhuang Coal Industry Co., Ltd., Changzhi 046000, China; 13994206821@163.com
[4] Korla Jinchuan Mining Co., Ltd., Korla 841000, China
* Correspondence: ckpyuew@163.com (Y.P.); zhouyafei25400@163.com (Y.Z.)

Abstract

In order to enable safe pillarless mining in a deep, thick coal seam with a hard roof, an integrated approach combining presplitting roof blasting and a flexible formwork concrete support system was implemented and evaluated via theoretical analysis, numerical simulation, and field trials. The limit-equilibrium analysis indicated a minimum gob-side coal pillar width of approximately 6 m. A pumpable C40 flexible-formwork concrete was developed, achieving its design compressive strength within 28 days, to serve as a roadside support. Field implementation of the presplitting and composite support effectively controlled roadway deformation: total roof–floor convergence was limited to 340 mm (floor heave accounted for 65%), and support loads remained within safe ranges, with no structural failures observed. These results demonstrate that the proposed gob-side entry retaining technique maintains roadway stability without a coal pillar, offering a practical and economic solution for deep coal mines with hard roofs.

Keywords: deep-buried thick coal seam; pillar-less mining; surrounding rock stability; deep-hole directional presplitting blasting; composite support system

Academic Editor: Francesca Dezi

Received: 8 June 2025
Revised: 11 July 2025
Accepted: 22 August 2025
Published: 2 September 2025

Citation: Ma, C.; Pan, Y.; Zhou, F.; Zhou, Y. Deformation Characteristics of Narrow Coal Pillar Roadway Incorporating the Roof Cutting Technique. *Infrastructures* **2025**, *10*, 231. https://doi.org/10.3390/infrastructures10090231

1. Introduction

Pillar-less mining is an advanced coal extraction method that eliminates traditional protective coal pillars by optimising mine layouts, excavation techniques, and roadway positioning [1,2]. Its core principle is to arrange roadways along goaf edges or within stress-relief zones to avoid stress concentrations typically associated with pillar retention [3]. Initially developed in the Soviet Union in the 1930s and subsequently improved worldwide [4], Pillar-less mining has become an essential direction in coal mining. It reduces the risk of dynamic disasters such as rockbursts and coal-and-gas outbursts by eliminating pillar-induced stress concentrations [5,6]. Additionally, this method minimises resource loss, improves coal recovery rates, and extends mine operational lifespans [7]. It also reduces roadway excavation, easing production scheduling conflicts. In high-gas mines, Pillar-less mining facilitates improved ventilation through Y-type ventilation arrangements, effectively controlling gas concentrations [8,9]. Moreover, this approach avoids isolated working faces, significantly enhancing overall mine safety and economic performance [10,11]. Consequently, Pillar-less mining is recognised as a crucial technology for achieving green and efficient coal resource extraction [12].

Gob-side entry retaining (GER), a critical technique supporting pillar-less mining, has evolved significantly since its initial application in the 1950s [13]. Early implementations in China involved waste-rock walls along thin-seam entries and internal timber supports. However, the significant compression of waste-rock walls, severe deformation of timber frames, slow manual construction, and low safety constrained its broader application. The design at this stage was passive, failing to accommodate dynamic rock deformation [14].

From the 1960s to the 1970s, advancements in mining technologies led to the adoption of dense timber props, timber packs, and waste-rock belts as roadside supports in medium-thick seams, accompanied by trapezoidal I-beam sets internally [15]. Although these methods provided improved stability, they lacked sufficient initial resistance and yielded inadequately under load, limiting their suitability primarily to low-gas mining environments. During the 1980s and 1990s, widespread mechanised longwall mining encouraged the adoption of roadside filling techniques, such as yieldable U-steel supports and quick-setting high-water-content filling materials [16,17]. Despite these innovations, passive support systems remained insufficiently adaptive to large-section deformation, and the complexity and high cost of filling technologies caused a reduction in their popularity. During this period, theoretical advancements emerged, including the rock-beam inclination theory proposed by British researcher S. Smethurst and support models developed by Chinese researchers such as Sun Henghu and Guo Yuguang, laying the groundwork for subsequent technical breakthroughs [18]. Since 2000, the widespread adoption of bolt-mesh-cable support systems has marked a shift toward active support strategies [19]. High-pretension bolts and cables have significantly enhanced surrounding-rock self-bearing capacities and roadway stability. Roadside supports have also become increasingly mechanised and advanced, incorporating high-performance filling materials such as high-water and paste fills. For example, Changcun Mine of the Lu'an Group successfully retained large-section gob-side entries in thick seams using combined bolt-beam-mesh supports and high-water filling. Concurrent theoretical progress has furthered understanding, with Li Huamin proposing a three-stage roof movement model and Xie Wenbing employing numerical simulations to clarify rock deformation mechanisms, guiding support parameter optimisation.

Nowadays, coordinated design integrating internal and roadside supports has become central to gob-side entry retaining technologies. Internal support systems primarily employ bolts, meshes, and cables, often supplemented by hydraulic props. Roadside support methods vary widely, including columns, walls, and fill-based structures. Among these, filling-type supports have become mainstream due to their high resistance and excellent sealing performance. Paste-filling technology, which uses coal gangue as aggregate, has reduced costs by nearly 50% compared to traditional high-water materials while effectively controlling roof subsidence. Nevertheless, mismatched support parameters under complex geological conditions and theoretical developments lagging behind practice remain critical issues restricting broader application.

Utilising pumping techniques and flexible forms, it rapidly forms strong supporting structures and effectively integrates solid waste resources, such as coal gangue, promoting greener mining practices. Developing low-cost, high-performance filling materials and improving flexible-formwork concrete mechanics and construction processes will significantly enhance the practicality and economic viability of gob-side entry retaining [20,21]. Additionally, integrating intelligent monitoring and stress-relief technologies will enable more precise rock control under complex geological conditions, facilitating broader adoption and advancement of pillar-less mining technologies. However, previous studies have seldom addressed gob-side entry retention under deep, hard-roof conditions using an integrated approach of presplitting blast-induced roof cutting and flexible formwork concrete

support. This lack of established methodology for hard-roof, pillarless mining motivated our research.

This study adopts an integrated approach combining theoretical analysis, laboratory testing, numerical simulation, and field validation to develop a roof-cutting and support system capable of maintaining roadway stability without coal pillars. Key design parameters and a suitable high-strength backfill material are identified and verified, and the effectiveness of the proposed system is demonstrated through field trials. Each step builds upon the previous one to address the central question of maintaining roadway stability without coal pillars.

2. Engineering Geological Condition

2.1. Longwall Face Overview

Xiadian Coal Mine, located in Xiangyuan County, Shanxi Province, is a high-gas mine with simple geological and hydrogeological conditions. Current production targets the No. 3 coal seam of the Qinshui Coalfield. The outer section of Panel 3118 is positioned in the south-western corner of the lease and follows the strike of the seam for ≈268 m. An auxiliary intake airway (6 m wide × 3.2 m high) is driven ahead of the face and supported by a bolt–mesh–cable system. The No. 3 seam belongs to the middle–lower Shanxi Formation. It is ≈6 m thick, dips 0–14° (mean ≈ 7°), and lies 485–515 m below the surface. The firmness coefficient ranges from 0.8 to 1.2. A single persistent parting is present; bright coal dominates, with minor dull coal. Although the seam is stable and internally simple, its hard, poorly permeable roof demands high surrounding-rock stability. Figure 1 shows the panel layout, and Table 1 summarises roof-and floor-rock lithology. The roof and floor comprise simple stratigraphy but markedly different lithologies, strongly influencing rock-mass behaviour.

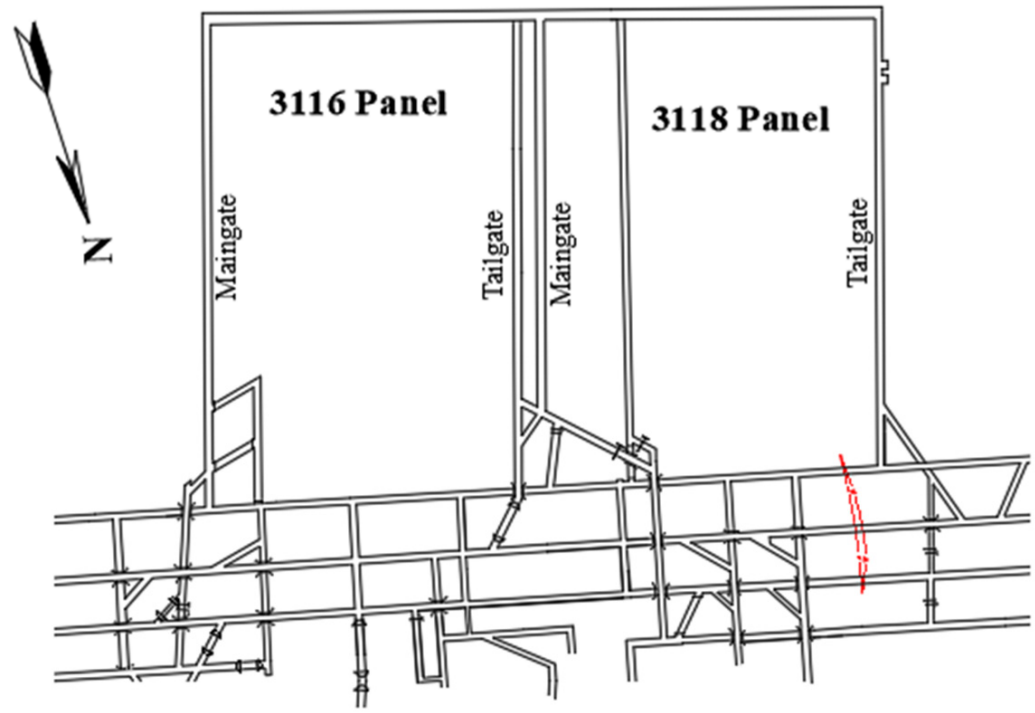

Figure 1. Layout of Panel 3118 and 3116.

Table 1. Lithological characteristics of the roof and floor of Panel 3118.

Stratigraphic Position	Rock Type	Lithological Description	Mean Thickness/m
Basic roof	Fine-grained sandstone/siltstone, interbedded	Light- to medium-grey, medium-thick beds; feldspar- and quartz-bearing sandy interlayers; thin sandy-mudstone layers with tabular cross-bedding	17.95
Immediate roof	Sandy mudstone	Dense, brittle; local plant fossils and coal debris; sandy content increases upward	1.2
No. 3 coal seam	Coal	Predominantly bright coal, massive black; minor dull coal	6
Immediate floor	Mudstone	Dense, brittle; lower part contains plant fossils and coal debris	2.75
Main floor	Fine-grained sandstone	Quartz- and feldspar-rich; dark minerals and sericite; muddy streaks, thick bedding, fissile	2

2.2. Physical and Mechanical Characterisation of Surrounding Rock

Exploration-borehole cores were tested for mechanical properties. The compressive strength of the No. 3 coal ranges from 10 to 15 MPa, averaging 13.85 MPa. Shallow excavation causes slight plastic damage in the ribs, but the coal mass remains generally intact. Roof mudstone and sandstone are far stronger; several sandstone specimens exceed 100 MPa.

2.3. In-Situ Stress Characteristics

Overcoring tests on floor cores from the Sanyi sector of Panel 3118, supplemented by numerical fitting, show a tectonically controlled stress field. Maximum horizontal stress is markedly greater than vertical stress. At Roadway 3108, for instance, the maximum horizontal stress is ≈18.30 MPa, whereas the vertical stress is ≈12.43 MPa. As shown in Table 2, good agreement between measured and calculated values confirms a stable regime dominated by horizontal tectonic components that govern stress redistribution during mining.

Table 2. Measured versus calculated in-situ stresses in the Sanyi sector.

No.	Station	Maximum Horizontal Principal Stress (MPa)		Minimum Horizontal Principal Stress (MPa)		Vertical Stress (MPa)	
		Meas.	Calc.	Meas.	Calc.	Meas.	Calc.
1	3121 haulage roadway (lower)	12.89	15.86	5.1	6.08	7.87	8.10
2	3121 haulage roadway (lower)	13.45	16.40	6.13	6.51	8.54	9.36
3	3121 gas-drainage roadway (left)	13.67	16.18	6.58	7.74	8.66	9.31
4	3123 haulage roadway	16.50	17.40	9.62	10.91	12.36	12.91
5	3113 auxiliary intake airway	10.15	11.3	6.4	7.41	11.63	12.53
6	3118 rail roadway	10.69	11.75	6.91	7.85	12.83	12.79
7	3113 haulage roadway	14.92	15.92	8.54	9.37	9.91	10.67
8	3108 haulage roadway	18.30	18.22	8.5	9.81	12.43	13.45

3. Theoretical Analysis

3.1. Mechanical Model

Ahead of and alongside the longwall face, abutment pressure induces a fractured–plastic zone in the coal rib (sidewall). Within this zone the coal mass attains a limit-equilibrium state. Because coal has a larger Poisson's ratio than the roof and floor rocks, and because the interface cohesion c_0 and internal-friction angle φ_0 are small, horizontal shear stresses develop along the coal-rock contacts and push the limit-equilibrium zone toward the roadway. For analytical clarity, the coal rib is idealised as a pillar of height m and unit thickness (Figure 2). The interface stress system comprises:

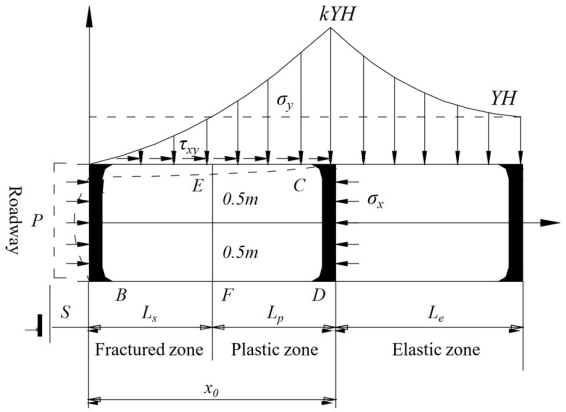

Figure 2. Stress model for the coal-rib/roof-floor interfaces.

P_i—horizontal reaction supplied by the support system;

σ_x—average horizontal stress at $x = x_0$ across the full rib thickness;

σ_y—vertical (longitudinal) stress within the rib.

This representation is the basis for determining the width of the limit-equilibrium zone and related parameters.

For clarity, the key parameters in this model are defined as follows:

γ—bulk density;

H—overburden depth;

k—vertical stress concentration factor (the ratio of the vertical stress at x_0 to the weight of the overlying strata, γH);

A—lateral pressure coefficient (the ratio of horizontal stress to vertical stress at x_0);

c_0—cohesion along the coal-rock interfaces (roof and floor);

φ_0—internal friction angle along the coal-rock interfaces (roof and floor).

These interface strength parameters are typically lower than the strength of the coal mass itself due to the weaker bonding at the coal-rock contacts [22].

3.2. Stress and Displacement in the Limit-Equilibrium Zone

The following assumptions apply:

1. Cohesion and internal-friction angle on the potential sliding surface are c_0 and φ_0.
2. Stresses in the rib are symmetric about the horizontal axis (i.e., about a horizontal plane through the mid-height of the coal seam, assuming the roadway lies approximately centrally within the seam so that the stress distribution is roughly symmetric).
3. At the boundary between the limit-equilibrium zone and elastic host rock

$$\sigma_y|_{x=x_0} = k\gamma H,\ \sigma_x|_{x=x_0} = Ak\gamma H \tag{1}$$

If P_0 is the horizontal force acting on interface CD, the net horizontal force on zone ABCD is

$$P = P_0 - P_i = mAk\gamma H - P_i \tag{2}$$

Under this horizontal force and the overburden load, the rib undergoes elastic and plastic deformation. Neglecting creep, the total displacement in the plastic stage is

$$S_1 = S_e + S_s \tag{3}$$

where S_e and S_s are the elastic and shear components, respectively.

As illustrated in Figure 3, let q denote the shear-stress gradient per unit length in the coal mass. Force equilibrium for an elemental slice then gives

$$q = -\frac{dP(x)}{dx} \tag{4}$$

where $P(x)$ is the axial force acting on an arbitrary cross-section S' of unit roadway width.

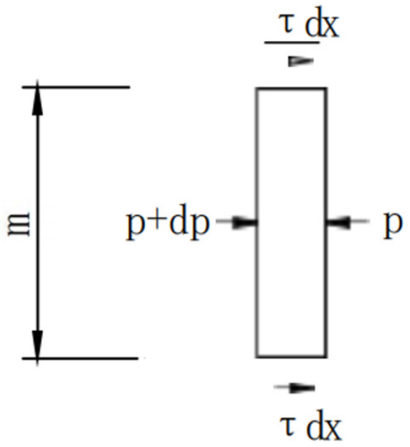

Figure 3. Elemental stress-displacement model for the coal mass.

According to Hooke's law,

$$P(x) = S' \times \sigma(x) = mE\frac{dS_e}{dx} \tag{5}$$

where E is the composite elastic modulus of the coal.

Substituting Equation (5) into Equation (4) yields the shear-stress gradient:

$$q = -mE\frac{d^2S_e}{dx^2} \tag{6}$$

Assuming the shear stress at the coal–rock interface varies linearly with the corresponding shear displacement,

$$q = 2 \times 1 \times \tau = K_s S_s \tag{7}$$

where K_s is the tangential stiffness of the interface—that is, the shear stress generated per unit shear displacement on a unit length of interface. This linear interface behaviour is a first-order approximation of the actual coal-rock interaction for small displacements, and is adopted here due to the lack of significant slip at the interface in the initial deformation stage.

Applying the boundary conditions provides closed-form solutions for shear displacement and stress throughout the limit-equilibrium zone; the interface shear stress obeys

$$\tau(x) = c_0 + \sigma_y tan\varphi_0 \tag{8}$$

Combining these expressions yields the vertical stress in the limit-equilibrium zone,

$$\sigma_y = \left[\frac{P\sqrt{\beta}}{2}\frac{ch(\sqrt{\beta}x)}{sh(\sqrt{\beta}x_0)} - c_0\right] \times cot\varphi_0 \tag{9}$$

and the elastic displacement S_e,

$$S_e = -\frac{P}{mE\sqrt{\beta}}\frac{cosh(\sqrt{\beta}x_0) - cosh(\sqrt{\beta}x)}{sinh(\sqrt{\beta}x_0)} \tag{10}$$

At the roadway side $S_e|_{x=x_0} = 0$, the elastic and shear displacements are

$$S_S|_{x=0} = \frac{-P}{mE\sqrt{\beta}sinh(\sqrt{\beta}x_0)} \tag{11}$$

$$S_e|_{x=0} = -\frac{P}{mE\sqrt{\beta}}\frac{2cosh(\sqrt{\beta}x_0) - 2}{sinh(\sqrt{\beta}x_0)} \tag{12}$$

giving the total displacement,

$$S_1 = \frac{-Ak\gamma H}{E\sqrt{\beta}}\left[2coth\left(\sqrt{\beta}x_0\right) - csch\left(\sqrt{\beta}x_0\right)\right] \tag{13}$$

Relative roof-floor convergence squeezes additional coal into the roadway. Neglecting coal compressibility, the extruded cross-section equals the area lost within the limit-equilibrium zone. If the maximum roof convergence is Δm, this additional displacement is

$$S_2 = -\frac{\Delta m}{m - \Delta m}x_0 \tag{14}$$

where m is the design roadway height.

The total rib displacement is therefore

$$S = \frac{-Ak\gamma H}{E\sqrt{\beta}}\left[2coth\left(\sqrt{\beta}x_0\right) - csch\left(\sqrt{\beta}x_0\right)\right] - \frac{\Delta m}{m - \Delta m}x_0 \tag{15}$$

In summary, the inward movement of the coal rib is directly proportional to the lateral-pressure coefficient A and the stress-concentration factor k, and inversely proportional to the composite elastic modulus E.

3.3. Deformation and Failure Analysis of the Coal Rib

Depending on coal-mass properties, two cases are considered for the width of the limit-equilibrium zone:

Plastic condition (soft coal with low brittleness)—the rib undergoes only plastic deformation under roof loading, and the width of the crushed zone L_s is zero. At interface EC, the shear stress satisfies

$$\tau(x)|_{x=x_0} = -(c_0 + k\gamma H tan\varphi_0) \tag{16}$$

from which the limit-equilibrium width is

$$x_0 = \frac{1}{2\sqrt{\beta}} ln \frac{2(c_0 + k\gamma H tan\varphi_0) + P\sqrt{\beta}}{2(c_0 + k\gamma H tan\varphi_0) - P\sqrt{\beta}} \tag{17}$$

Equation (17) confirms that under purely plastic conditions (no crushed zone), the limit-equilibrium width x_0 increases linearly with the applied horizontal force P. In contrast, when the vertical stress from the roof exceeds the coal's strength, a crushed zone will form at the rib surface. If the stress stays below that strength, the rib undergoes only plastic deformation without a crushed zone. For instance, at the No. 3 coal seam, the uniaxial compressive strength of the coal is about 13.85 MPa. Given a roadway depth of 500 m, the vertical stress at the elastic-plastic boundary is approximately $k\gamma H$ (with $k \approx 2$ and $\gamma \approx 26$ kN/m^3), which is on the order of 26 MPa—approaching or exceeding the coal strength. This means that under high abutment pressure, the coal rib can indeed enter a crushed state. Conversely, under lower stress or with effective support, the deformation remains primarily plastic and no obvious crushed zone develops.

At interface *EF*, the boundary condition is

$$\sigma_y|_{x=L_s} = \gamma H \tag{18}$$

and simultaneous solution of Equations (9) and (18) gives the crushed-zone width,

$$L_s = \frac{1}{\sqrt{\beta}} ln\left(B + \sqrt{B^2 - 1}\right) \tag{19}$$

with the remaining plastic width,

$$L_p = x_0 - L_s \tag{20}$$

3.4. Parametric Analysis

To reflect actual mining conditions, the factors influencing the width of the limit-equilibrium zone under the plastic (non-crushed) scenario are analysed. For simplicity, let $P_i = 0$. Relevant parameters are defined as follows:

$$K_s = 0.12 \text{ GPa/m},\ m = 3 \text{ m}, E = 3.2 \text{ GPa}, k = 2, \gamma = 26 \text{ kN/m}^3$$

Specifically, the coal's elastic modulus E was obtained from laboratory tests on the coal seam, and parameters like the stress concentration factor k were selected based on in situ stress measurements or well-established empirical values in deep mining [23,24].

Substituting these symbols into Equation (17) gives

$$x_0 = 4.472 ln \frac{2 + \frac{0.0174408AH}{c_0 + 0.052Htan\varphi_0}}{2 - \frac{0.0174408AH}{c_0 + 0.052Htan\varphi_0}} \tag{21}$$

Equation (21) shows that the limit-equilibrium width x_0 increases slowly but continuously with roadway depth H (Figure 4). The coloured curves indicate different rock conditions: the red line represents a stable condition (e.g., c_0 = 0.8 MPa, φ_0 = 30°, A = 0.6), the green line a moderately stable condition (e.g., c_0 = 0.5 MPa, φ_0 = 25°, A = 0.6), and the blue line an unstable condition (e.g., c_0 = 0.3 MPa, φ_0 = 16°, A = 0.4). These interface cohesion and friction values fall within the range reported from laboratory direct shear tests on coal-rock interfaces, which supports the choice of parameters [25].

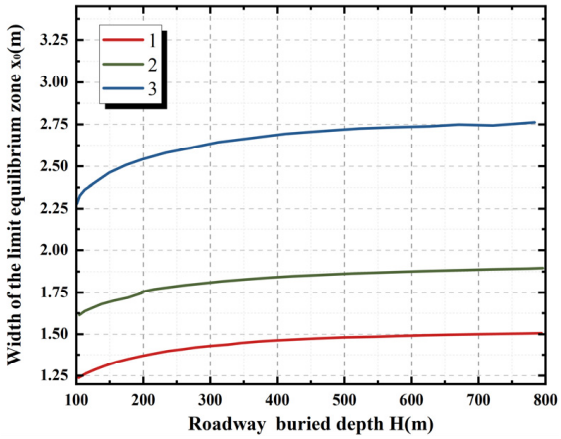

Figure 4. Relationship between limit-equilibrium width and roadway depth.

Increasing the friction angle φ_0 raises the shear strength of the coal-rock interface but decreases x_0. For example, when $\varphi_0 = 15^{\circ}$, the calculated x_0 is 3.25 m. Vertical-stress distributions for various φ_0 values, obtained from Equation (8), are plotted in Figure 5.

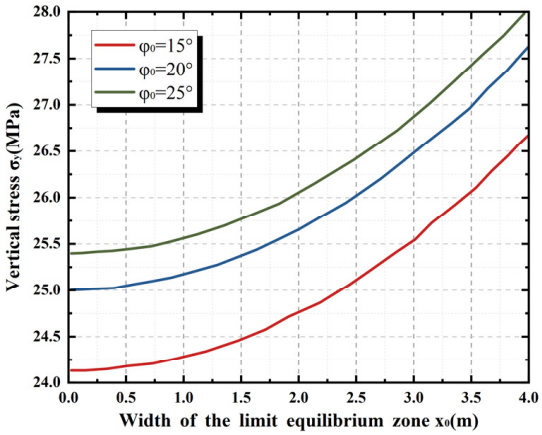

Figure 5. Vertical-stress profiles in the limit-equilibrium zone for different interface-friction angles.

A higher cohesion c_0 likewise raises σ_y yet reduces x_0 (Figure 6).

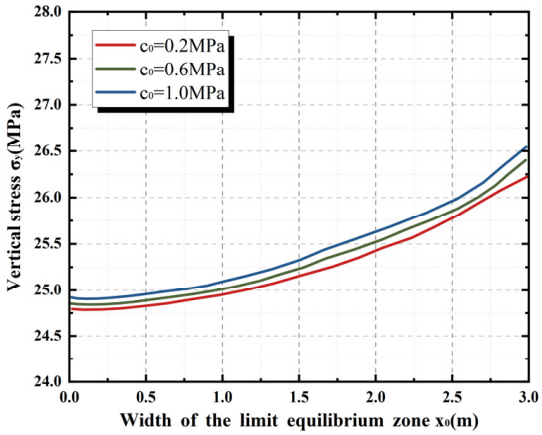

Figure 6. Vertical-stress profiles for different interface cohesions.

A greater roadway height m enlarges x_0 (Figure 7), indicating that higher entries develop wider plastic zones under otherwise identical conditions.

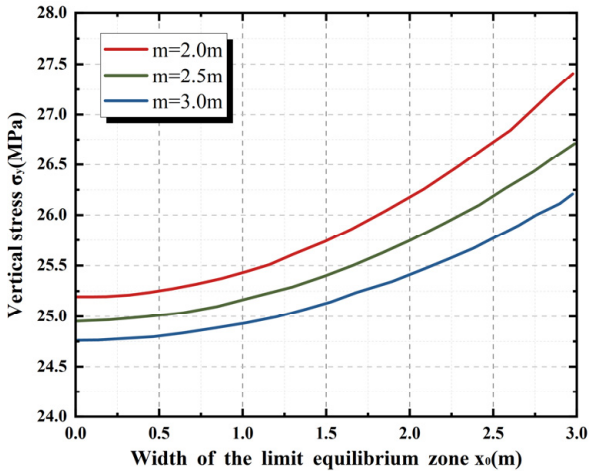

Figure 7. Effect of roadway height on the vertical-stress profile.

The inward displacement of the coal rib is proportional to the lateral-pressure coefficient A and stress-concentration factor k, and inversely proportional to the composite elastic modulus E.

The limit-equilibrium width x_0 depends on roadway depth H, overburden unit weight γ, interface strength parameters (c_0, φ_0, K_s), stress-concentration factor k, lateral-pressure coefficient A, roadway height m, and elastic modulus E. Specifically, x_0 decreases with increasing φ_0 and c_0 but increases with H and m.

When x_0 exceeds the anchorage length of bolts and cables, rib deformation manifests mainly as pronounced inward movement, yet bolt/cable failure is rare. Conversely, if x_0 is shorter than the anchorage length and the lateral pressure exceeds the shear resistance of the reinforcement, splitting of the rib and shearing of bolts/cables can occur. If the lateral load is lower, the rib remains stable. Existing bolt-only support is not sufficient to restrain severe rib spalling; thus cable bolts longer than 4 m are required to control large deformations effectively.

4. Materials and Experimental Programme

4.1. Concrete-Mix Design Tests

The purpose of the mix design and compressive strength testing is to ensure that the chosen backfill material (C40 concrete) possesses sufficient mechanical strength to serve as a reliable roadside support, thereby underpinning the stability of the retained roadway.

The cement used was ordinary Portland cement (OPC) with a grade of 42.5 MPa, ensuring the potential to reach the C40 strength class. The fine aggregate was a well-graded medium river sand (fineness modulus 2.6–3.0), and the coarse aggregate was a crushed stone of 5–20 mm size. Both aggregates were clean (low fine content) and continuously graded, which helps improve the concrete's workability and density. The mixed water was clean (settled and filtered mine water). A polycarboxylate-based high-range water-reducing admixture was added to enhance workability and pumpability without increasing the water content. This admixture was specifically chosen for its effectiveness in pumped concrete applications.

Workability was assessed by slump and slump-flow tests on a purpose-built platform (Figure 8). An L9 orthogonal experimental design was adopted, varying four factors—mixing water, water-to-cement (w/c) ratio, coarse-aggregate fraction, and powder fraction—each at three levels (Table 3). Factor ranges were established in accordance with mix-design guidelines and existing research [26,27]. Specifically, w/c ratios from 0.45 to 0.50 were examined. Although C40 concrete conventionally requires w/c $\leq$ 0.45 for strength, ratios

up to 0.50 were included to secure pumpable workability. Water contents of 180–200 kg were selected to achieve a target slump of 230–250 mm, while coarse-aggregate and powder proportions were set at 0.50–0.60 and 0.45–0.50, respectively, to cover practical limits that ensure adequate flow without segregation. This orthogonal matrix facilitates systematic evaluation of each parameter's influence on workability and compressive strength.

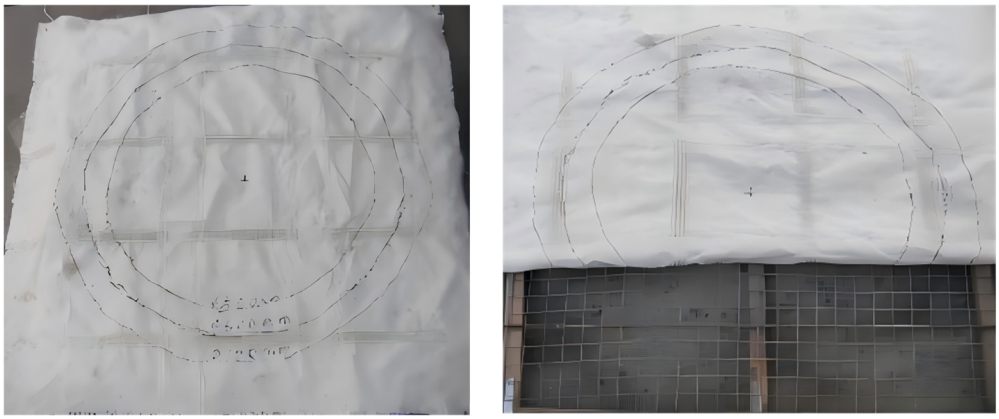

Figure 8. Platform for slump and slump-flow testing.

Table 3. Slump and slump-flow results.

Test	Water (kg)	w/c	Coarse-Aggregate Ratio	Powder Ratio	Slump (mm)	Flow (mm)
1	180	0.45	0.5	0.45	220	540
2	180	0.47	0.55	0.47	225	580
3	180	0.50	0.60	0.50	230	595
4	190	0.45	0.55	0.50	225	550
5	190	0.47	0.60	0.47	240	585
6	190	0.50	0.50	0.45	245	595
7	200	0.45	0.60	0.47	235	585
8	200	0.47	0.50	0.50	245	590
9	200	0.50	0.55	0.45	250	600

Range and variance analyses (Table 4) identified the most influential factors.

Table 4. Range analysis of slump and slump-flow.

Item		Σ (level)				Mean/Range			
		A	B	C	D	A	B	C	D
Slump/mm	K1	675	680	710	710	225.0	226.7	236.7	236.7
	K2	710	710	700	705	236.7	236.7	233.3	235.0
	K3	730	725	705	700	243.3	241.7	235.0	233.3
	$\overline{R}$					18.3	15.0	3.3	3.3
Flow/mm	K1	1715	1675	1725	1725	571.7	558.3	575.0	575.0
	K2	1730	1755	1730	1760	576.7	585.0	576.7	586.7
	K3	1775	1790	1765	1735	591.7	596.7	588.3	578.3
	$\overline{R}$					20.0	38.3	13.3	11.7

Considering the above factors, the recommended proportions are: water 225 kg/m^3, w/c 0.45, cement 500 kg/m^3, coarse-aggregate ratio 0.60, sand-in-mortar ratio 0.45.

Field aggregates contain variable moisture, so the laboratory mix was adjusted for site conditions. Underground pumping trials confirmed acceptable workability. Field

pumping trials with this mix were conducted in a borehole at the site, confirming its adequate workability for underground placement. The mix's measured slump (230–250 mm) ensured it could be pumped over the required distance without segregation. The final C40 construction mix is shown in Table 5.

Table 5. Construction mix for C40 concrete.

Component	Cement	Water	Sand	Coarse Aggregate
kg/m^3	750	382	900	900

4.2. Compressive-Strength Test of Concrete

Concrete cubes (150 mm × 150 mm × 150 mm) were cast in accordance with the Standard Test Methods for Concrete, with three specimens per batch. Moulds were coated with release agent, filled with concrete mixed to the target proportions, and struck off after slump measurement. After 24 h the specimens were demoulded, labelled, and cured at ambient temperature until the designated ages. They were then tested for compressive strength at an accredited laboratory, yielding complete strength–age curves. This strength satisfies the design criteria for the backfill (≥40 MPa at 28 days for C40 grade), indicating that the concrete wall will have the capacity to withstand the anticipated loads from the surrounding rock. In later sections, this chosen material strength directly contributes to the excellent stability observed in the field.

4.3. Stability Analysis of the Roadside Concrete Wall

A flexible-formwork concrete wall serves as the primary support along the gob-side entry. Failure occurs when the applied stress reaches the wall's ultimate capacity or deformation exceeds the allowable limit, similar to rock failure under uniaxial compression. As mentioned in Figure 9, typical modes include (i) shear failure, (ii) longitudinal splitting, (iii) failure along weak planes or faults, and (iv) bulging after the wall is forced into the floor.

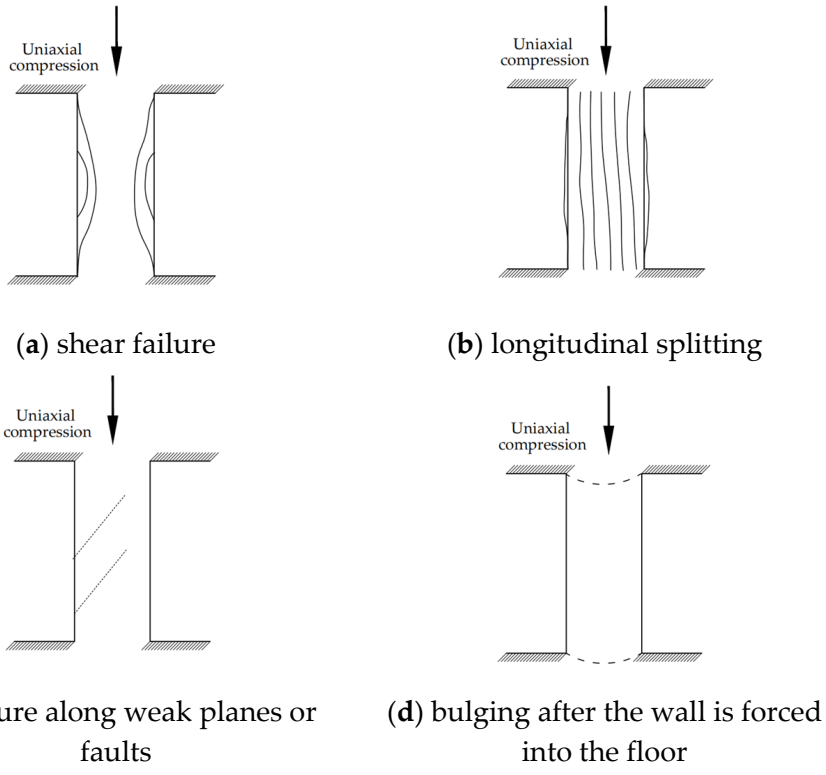

(**a**) shear failure (**b**) longitudinal splitting

(**c**) failure along weak planes or faults (**d**) bulging after the wall is forced into the floor

Figure 9. Typical failure modes of the concrete wall.

As illustrated in Figure 10, the concrete wall can operate in three distinct states. In the stable state, applied loads remain below the wall's ultimate capacity and no visible damage develops. In the partially failed yet stable state, some local failure (e.g., minor cracking or spalling of the concrete wall) has occurred. However, the support structure continues to carry the load with a sufficient margin of safety. In this state, the wall and bolts have yielded only locally, and their applied loads remain below the residual strength capacity—in other words, the support's factor of safety is still above 1.0—so the overall structure remains stable and intact. In the progressive failure state, either sustained loading or significant strength degradation reduces the residual capacity below the applied support pressure, causing failure to propagate until collapse. For practical roadway support, the design goal is to keep the wall within the second state, permitting limited plastic deformation while retaining adequate residual strength.

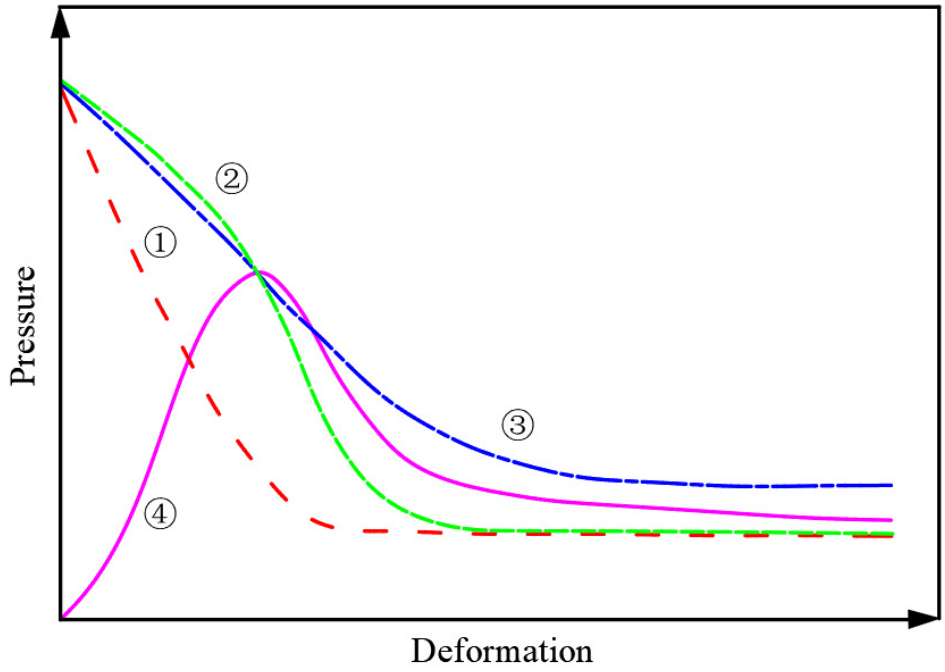

Figure 10. Three working states of the concrete wall.

Wall stability depends mainly on load magnitude and geometry. A larger width-to-height ratio places the wall core under triaxial compression, markedly improving compressive resistance. Accordingly, both the expected load and wall dimensions must be optimised to ensure stability during mining-induced disturbance.

5. Numerical Simulation

5.1. Numerical-Model Construction

The geological structure of the gob-side entry was simulated with FLAC3D, an explicit finite-difference code widely used for continuum analysis of rock and soil. Developed by ITASCA, FLAC can reproduce yielding, plastic flow, strain-softening and large deformation in geomaterials. A valid model requires a logical grid, appropriate constitutive laws, and well-defined initial and boundary conditions. The empirical parameters obtained from lab tests (rock and concrete properties) are used to build a FLAC3D numerical model. The simulation will help verify the theoretical findings under realistic conditions and optimise the support design before field implementation.

The model is based on the outer section of Panel 3118 in Xiadian Coal Mine. The face runs ≈268 m along strike; the coal seam is ≈6 m thick and geometrically stable. To simplify, the surrounding rock is treated as stratified, homogeneous, and isotropic elastic media. The initial stress field is assumed hydrostatic and calculated from the mean burial depth. Model dimensions are 200 m (strike) × 80 m (height) × 60 m (dip width). The 6 m-thick seam, with its floor at 20 m depth, is sandwiched by mudstone and sandstone roof and floor strata. Horizontal displacements are fixed on all vertical boundaries; vertical displacement is fixed at the base; the top surface carries a uniform load of 9.91 MPa representing overburden weight. Mechanical parameters are listed in Table 6, and the mesh is shown in Figure 11. These settings provide the baseline for subsequent analyses.

Table 6. Rock and backfill mechanical parameters.

Lithology	Bulk Modulus /GPa	Shear Modulus /GPa	Density/kg/m^3	Cohesion/MPa	Friction Angle/°	Tensile Strength/MPa
Mudstone-fine-sandstone interbeds	6.30	4.80	2700	3.51	34	4.3
Fine sandstone	8.70	4.2	2480	2.98	31	5.21
Sandy mudstone	6.46	2.45	2320	1.72	28	2. 1
Coal seam	1.60	1.40	1440	3.42	33.1	3.75
Sandy mudstone (lower)	6.46	2.45	2320	1.72	28	2.2
Fine sandstone (lower)	9.70	3.10	2230	2.64	30	4.91
Backfill concrete	13.89	5.3	2500	3.2	30	4.32

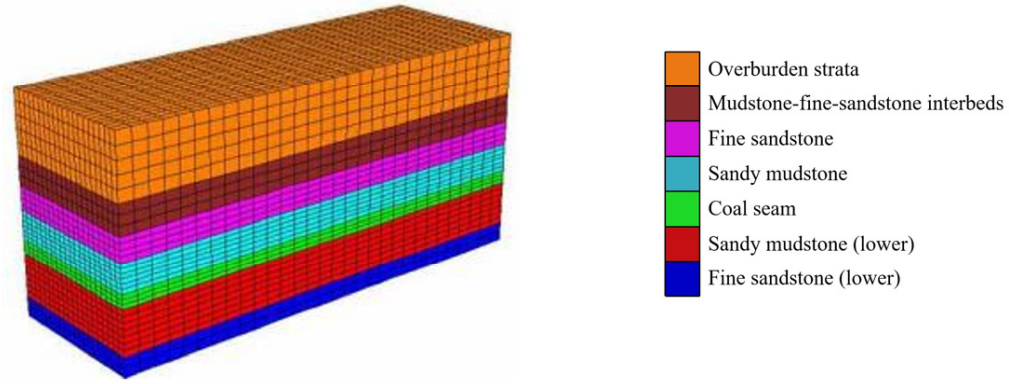

Figure 11. Numerical model used for FLAC3D analysis.

5.2. Simulation Results and Analysis

FLAC3D was further used to model three successive stages—roadway excavation, longwall retreat, and gob-side entry retaining. Key findings are summarised below.

(i) Roadway-excavation stage (before retreat)

The stress cloud plot is shown in Figure 12. After excavation, vertical stress near the immediate roof and floor drops to very low values, whereas the two coal-rib pillars experience pronounced concentration. The maximum vertical stress reaches 22.4 MPa; under the action of support, this peak shifts deeper into the ribs. The peak horizontal stress is 10.97 MPa and likewise migrates into the roof- and floor-rock mass. The maximum shear stress is 3.15 MPa, concentrated around the shoulder corners. Overall, the stress field is symmetric and ordered, favouring roadway stability.

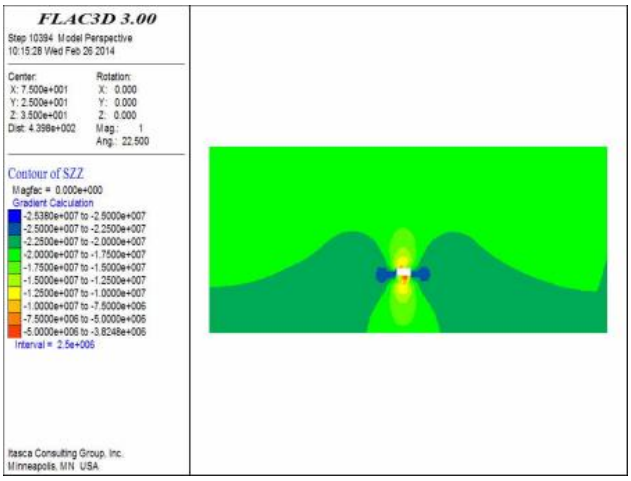

(**a**) vertical-stress contour map

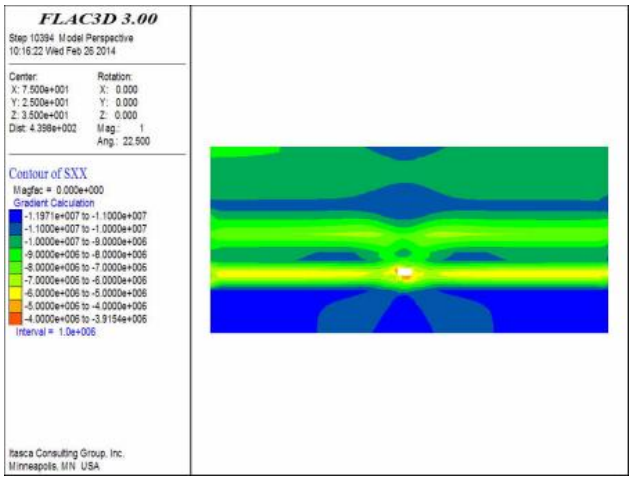

(**b**) horizontal-stress contour map

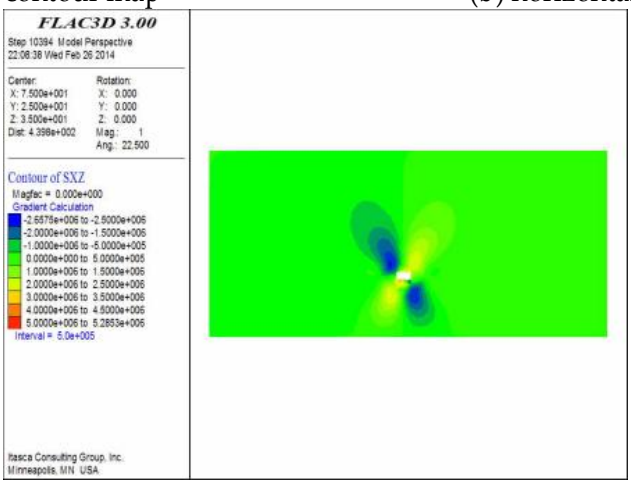

(**c**) shear-stress contour map

Figure 12. Stress distribution around the roadway immediately after excavation. (Central white rectangle in the figure indicates the roadway).

(ii) Mining-influence stage.

Once retreat is simulated, the development of the goaf produces a pronounced, asymmetrical redistribution of stress. In the area behind the face, removal of the coal causes the roof and floor to unload. Vertical stress therefore decreases step-wise with depth, while the high-stress zone on the gob-side rib expands relative to the pre-mining condition. Along the retreat direction, vertical stress in the roof and floor inside the goaf rises gradually; the peak ahead of the face migrates deeper into the coal pillar, giving a support-pressure influence zone that extends more than 20 m. Conversely, in front of the face, mining shifts roof-rock vertical stress even farther into the strata and increases the peak value, which concentrates in the rib on the mining side. A similar trend is observed for horizontal stress (Figure 13): peaks move to greater depth, grow slightly in magnitude, and render the overall field distinctly biased toward the retreat side. The shear-stress field (Figure 14) likewise migrates toward both ribs and the roof; peak shear values rise sharply above those recorded after excavation, indicating an elevated risk of shear-induced deformation.

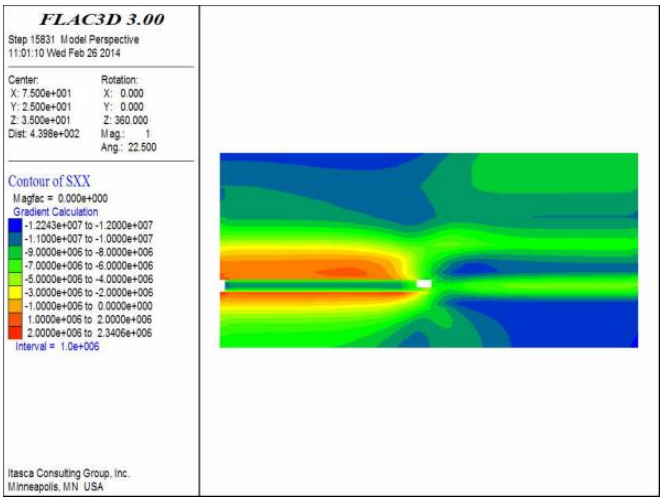

(**a**) horizontal-stress contour map at the lagging (behind-face) position

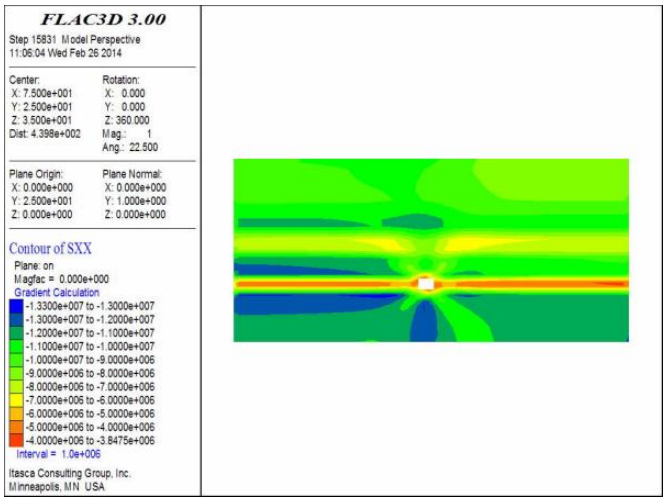

(**b**) horizontal-stress contour map at the leading (ahead-face) position

Figure 13. Horizontal-stress distribution during retreat.

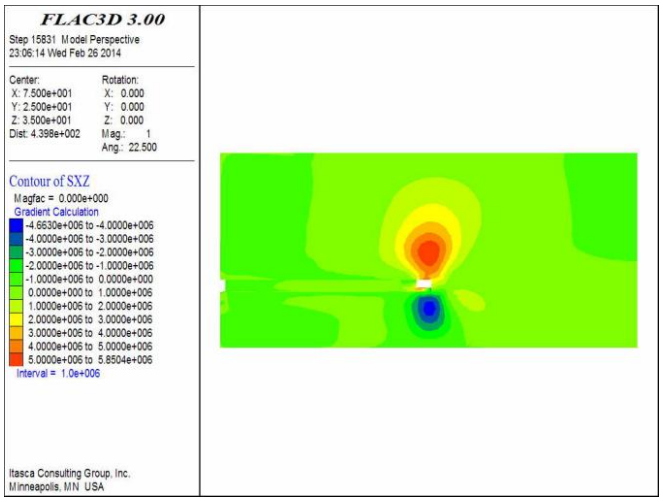

(**a**) shear-stress contour map at the lagging (behind-face) position

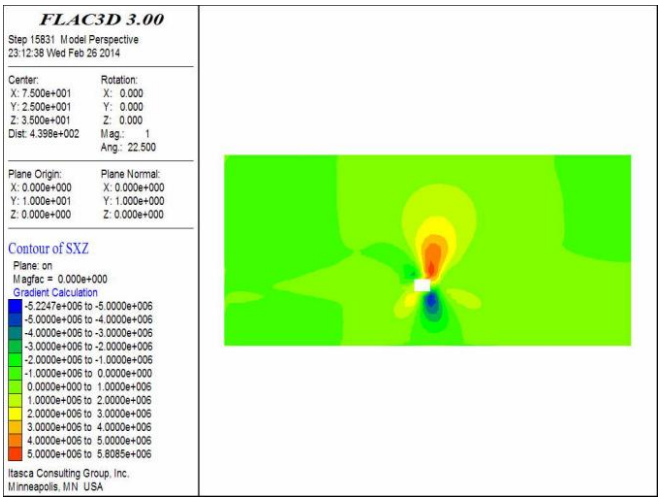

(**b**) shear-stress contour map at the working face

Figure 14. Shear-stress distribution during retreat. (Central white rectangle in the figure indicates the roadway).

(iii) Gob-side entry-retaining stage.

A 1.5 m-wide, C40 concrete backfill was introduced next to the roadway and analysed (Figure 15). The backfill itself bears high vertical stress—part transmitted from deeper strata, part transferred to the retained-roadway roof. Horizontal stress remains low in the rib/backfill zone, with peaks at the roof and rib edges. Shear stress concentrates at these edges, imposing large shear loads on both backfill and surrounding rock. Mining therefore disrupts the original symmetric field: most stress moves into deep rock, but a portion concentrates in the backfill, which could yield or destabilise.

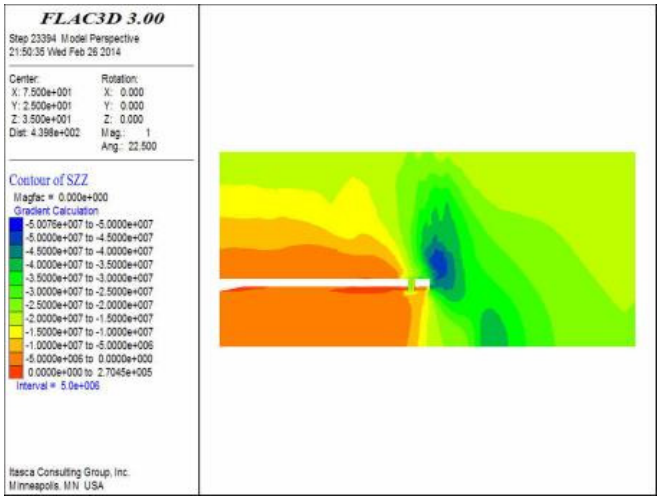

(**a**) vertical-stress contour map

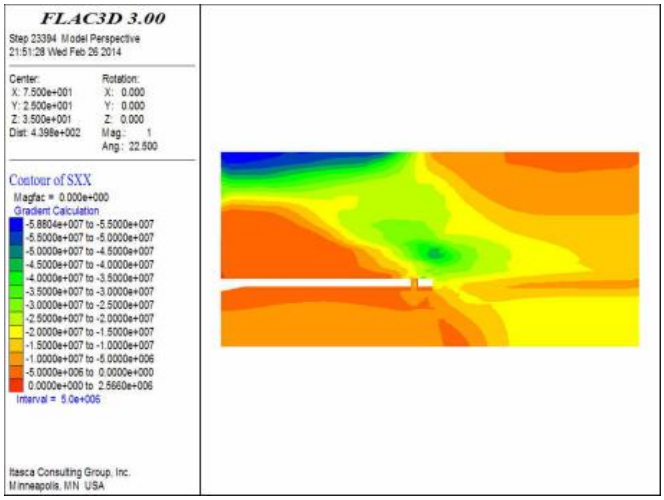

(**b**) horizontal-stress contour map

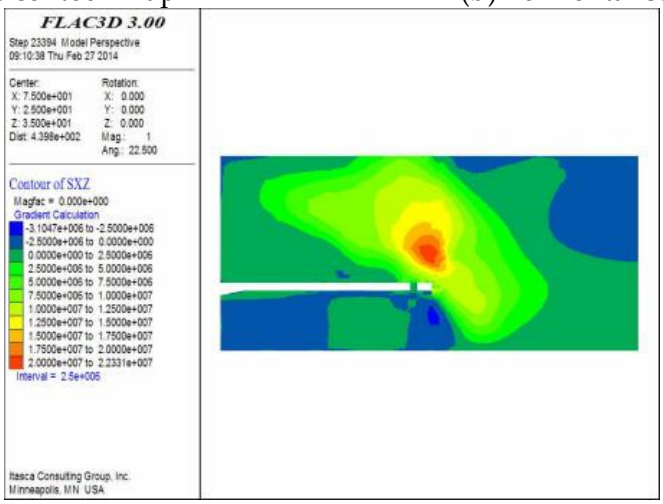

(**c**) shear-stress contour map

Figure 15. Stress distribution during gob-side entry retaining. (The left white rectangle represents the gob area, while the right white rectangle denotes the roadway).

(iv) Influence of backfill width.

Backfill widths ranging from 0.8 m to 2.0 m were evaluated to optimise the retained-entry design. The stresses in the surrounding rock changed little as width increased; however, the internal stresses of the backfill varied markedly. When the width grew from 0.8 m to 1.2 m, the maximum vertical stress inside the backfill fell steeply from about 20 MPa to roughly 15 MPa. Between 1.2 m and 1.8 m, this vertical stress remained nearly constant at 15 MPa but began to rise again once the width exceeded 1.8 m. A comparable trend was observed for horizontal stress: it dropped from 15 MPa to approximately 13.1 MPa in the 0.8–1.2 m range and then stabilised at about 13.2 MPa for wider fills. Shear stress declined from 3.85 MPa to around 3.3 MPa as width increased to 1.2 m, fluctuated near that level up to 1.8 m, and continued to decrease beyond this point. Collectively, these results indicate that a backfill width of 1.2–1.8 m keeps all three principal stresses in a low, stable range, minimises deformation of the backfill, and thereby best promotes the long-term stability of the gob-side entry (Figures 16–18).

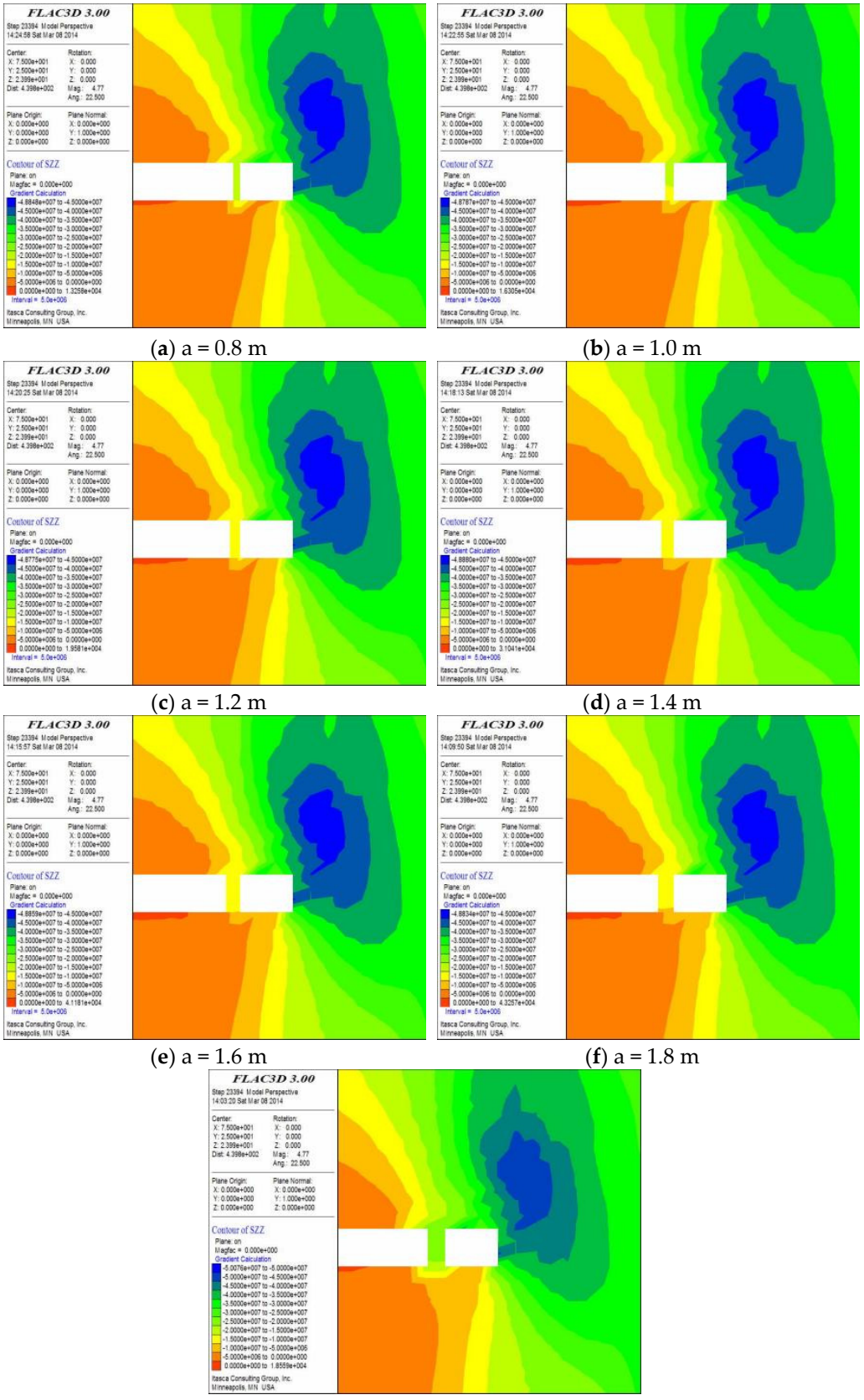

(**a**) a = 0.8 m (**b**) a = 1.0 m

(**c**) a = 1.2 m (**d**) a = 1.4 m

(**e**) a = 1.6 m (**f**) a = 1.8 m

(**g**) a = 2.0 m

Figure 16. Vertical stress versus backfill width. (The left white rectangle represents the gob area, while the right white rectangle denotes the roadway).

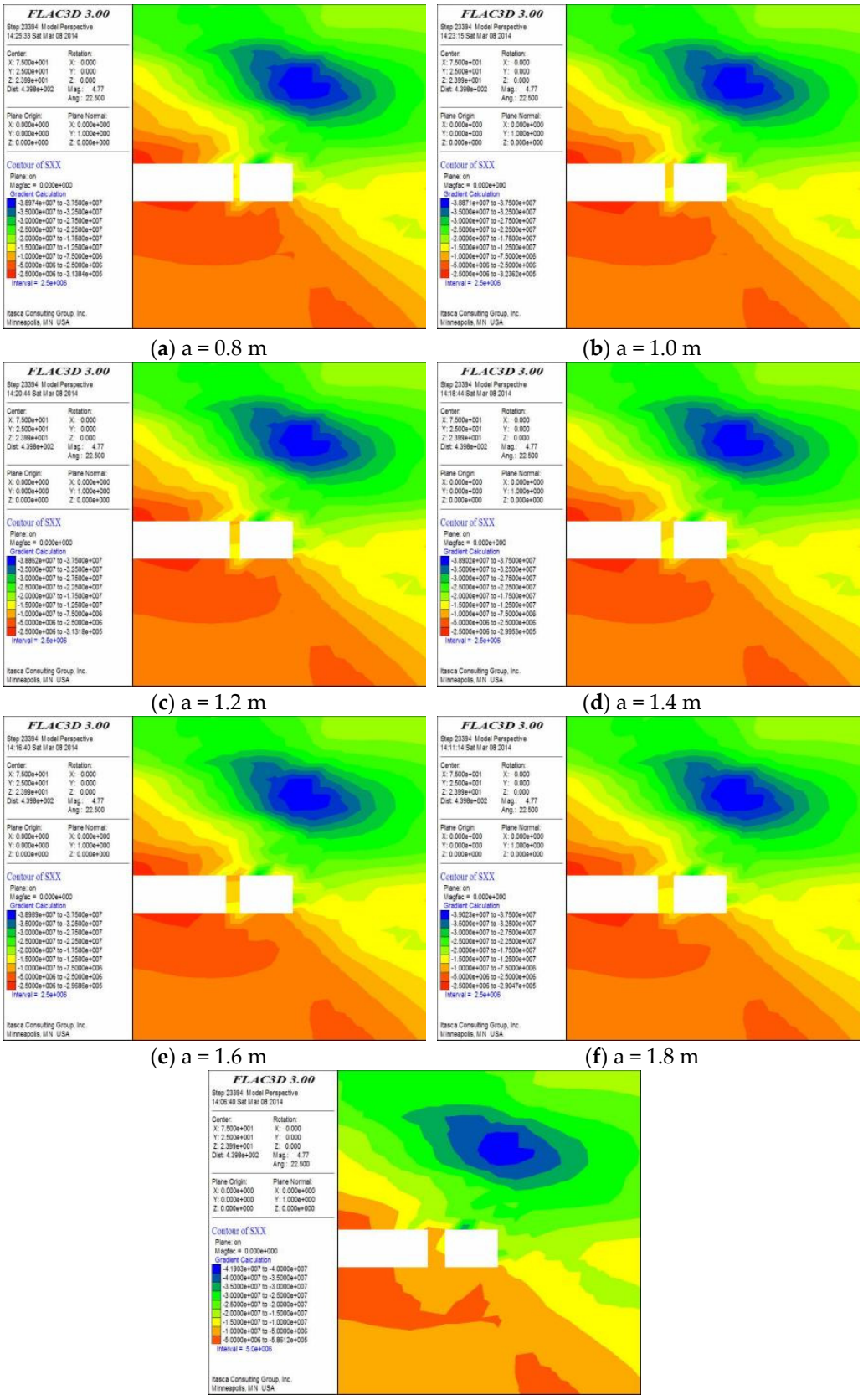

(**a**) a = 0.8 m (**b**) a = 1.0 m

(**c**) a = 1.2 m (**d**) a = 1.4 m

(**e**) a = 1.6 m (**f**) a = 1.8 m

(**g**) a = 2.0 m

Figure 17. Horizontal stress versus backfill width. (The left white rectangle represents the gob area, while the right white rectangle denotes the roadway).

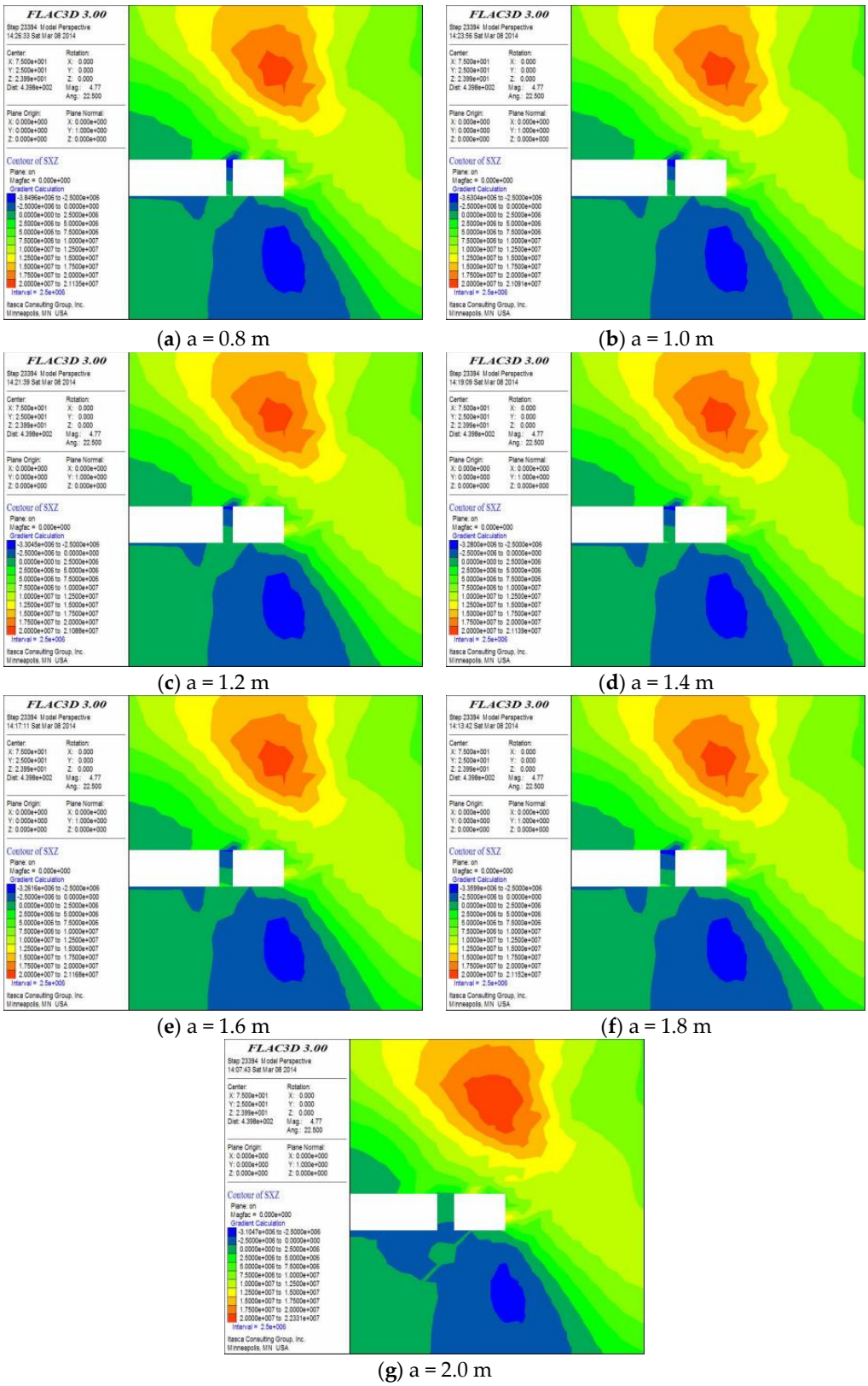

(**a**) a = 0.8 m (**b**) a = 1.0 m

(**c**) a = 1.2 m (**d**) a = 1.4 m

(**e**) a = 1.6 m (**f**) a = 1.8 m

(**g**) a = 2.0 m

Figure 18. Shear stress versus backfill width. (The left white rectangle represents the gob area, while the right white rectangle denotes the roadway).

6. Field Application

6.1. Deep-Hole Directional Presplitting

Prior to gob-side entry retaining in the auxiliary intake airway of Panel 3118, the roof was pre-split by deep-hole directional blasting. Optimised drilling parameters were: 60 mm borehole diameter, 75° inclination, 18 m hole length, 0.8 m spacing, 12 m charged section (6 m stemming), and 12 kg explosive per hole (Table 7). Emulsion explosives and "O-shaped" energy-concentrating tubes were used to achieve bidirectional focused blasting. After drilling, a borehole camera was employed to inspect fractures in the roof (Figure 19). Continuous cracks were observed from the bottom of the charged section to the hole collar, specifically at depths of 6.8–9.5 m, 11–13.8 m, 14–15.5 m, and 16–17.8 m; the cumulative crack length exceeded 70% of the blast section. The presplitting effectively weakened the roof, created a through-going fracture zone, and released mining-induced stress in advance. No significant roof damage or support failure was detected after blasting, indicating that the technique achieved its stress-relief objective without compromising surrounding support and thus provided a sound basis for subsequent safe entry retaining.

Table 7. Main blasting parameters.

Borehole Diameter	Hole Spacing	Hole Length	Hole Inclination	Charged Length	Explosive Per Hole	Linear Charge Density	Stemming Length
60 mm	800 mm	18 m	75°	12 m	12 kg	1.0 kg/m	6 m

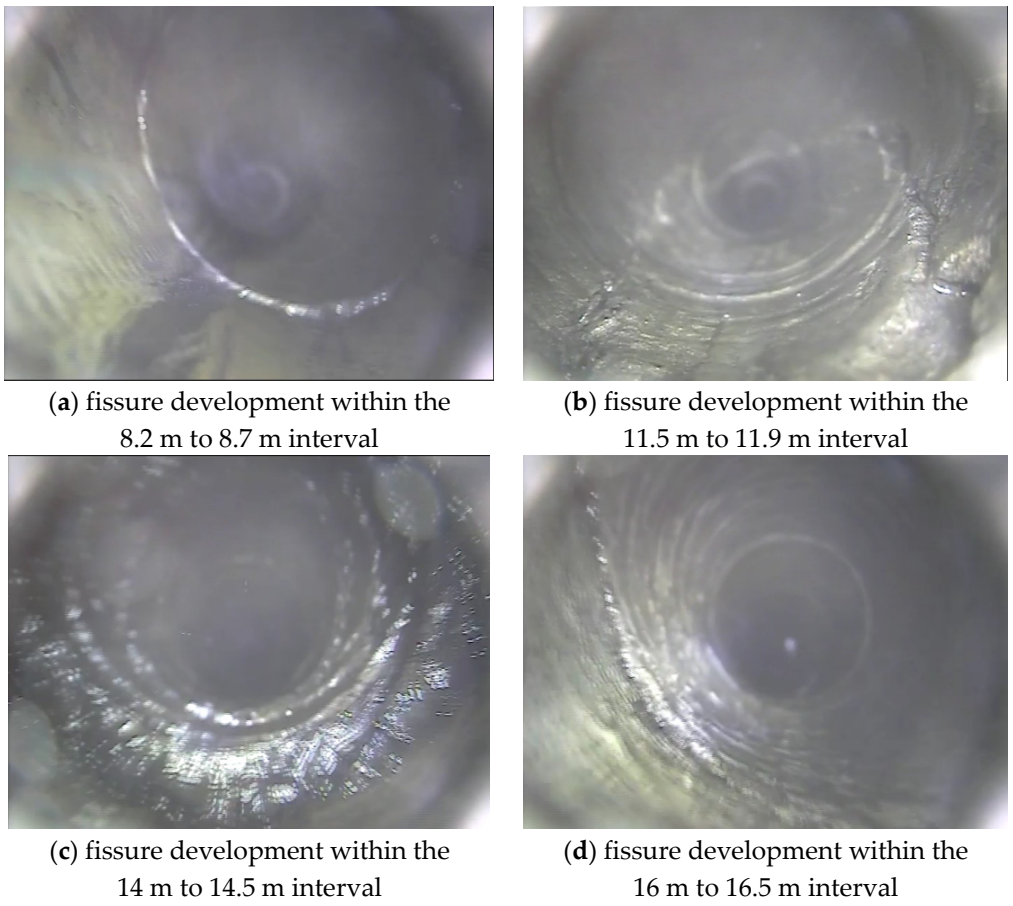

(**a**) fissure development within the 8.2 m to 8.7 m interval

(**b**) fissure development within the 11.5 m to 11.9 m interval

(**c**) fissure development within the 14 m to 14.5 m interval

(**d**) fissure development within the 16 m to 16.5 m interval

Figure 19. Borehole-camera image showing roof fractures after presplitting.

6.2. Anchor–Mesh–Cable Composite Support

An anchor–mesh–cable support system was installed along the retained entries—namely, the Panel 3118 auxiliary intake airway and the Panel 3121 return roadway (see Figure 20).

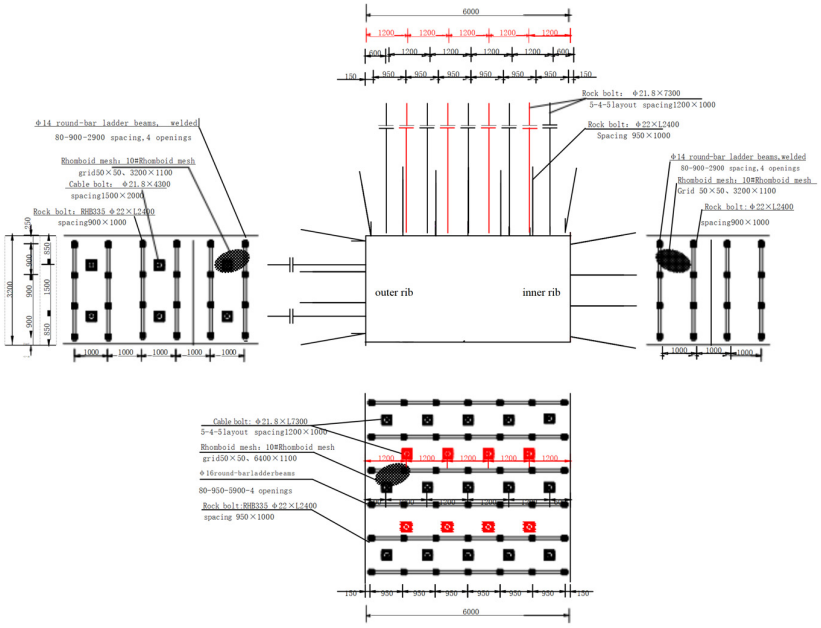

Figure 20. Support layout for the retained entries.

RHB335 rebar bolts (∅22 mm × 2400 mm) were installed at a spacing of 0.95 m × 1.00 m and pretensioned to 300 N·m, meeting the required anchorage capacity. Roof cables consisted of ∅21.8 mm × 7300 mm high-strength prestressed strands arranged in a 5-4-5 pattern at 1.20 m × 1.00 m spacing. Each cable was fitted with a 300 mm × 300 mm × 16 mm domed bearing plate and anchored with three resin cartridges (one CK2335 and two Z2360), providing an initial pretension of ≥250 kN.

Opposing-pair anchors (Figure 21) were installed through the backfill wall: RHB500 left-hand threaded bars, ∅22 mm × 1750 mm (for a wall thickness of 1500 mm), with thread lengths ≥150 mm on both ends, spaced at 0.80 m × 0.60 m and pretensioned to 300 N·m.

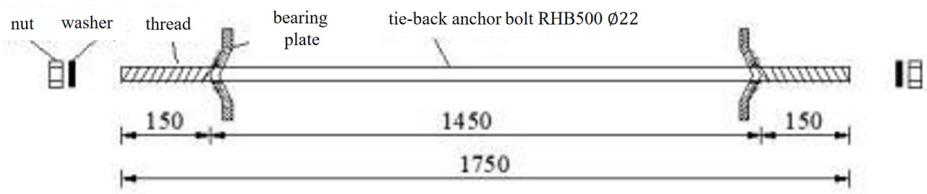

Figure 21. Geometry of opposing-pair anchors.

A ladder-shaped reinforcing beam was welded to connect upper and lower anchors (Figure 22), enhancing global stiffness. On the gob side of the entry, a three-dimensional flexible textile form (2400 mm × 1500 mm × 3500 mm; Figure 23) was erected and filled with C40 concrete, creating a rigid retaining wall. The lightweight, high-strength formwork simplifies construction and isolates the goaf roof effectively. Both ribs were additionally covered with wire mesh and arched steel plates to prevent spalling.

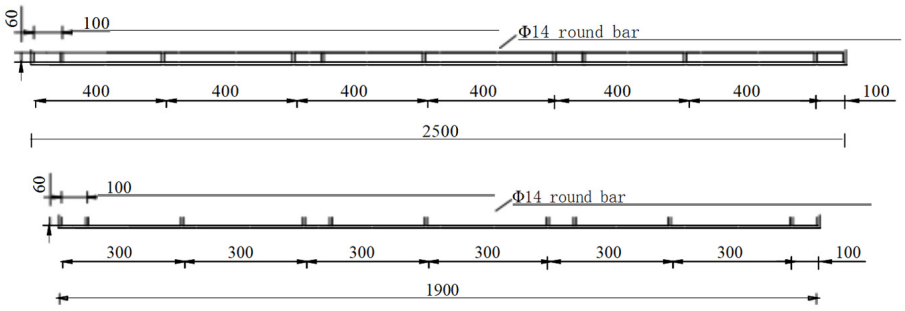

Figure 22. Dimensions of the ladder-shaped reinforcing beam.

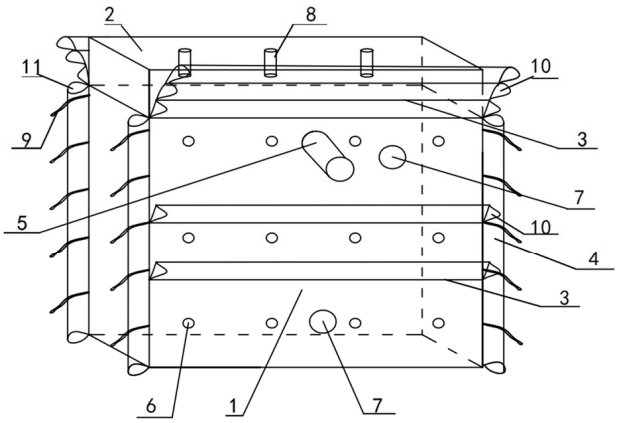

1-main formwork panel; 2- top- connection formwork panel; 3-central flange; 4-vertical flange; 5-grouting port; 6-anchor- bolt hole; 7-drainage (gas-extraction) hole; 8-rebar insertion opening; 9-connecting rope; 10- flange sleeve (for placing vertical reinforcement); 11-edge- flange

Figure 23. Three-dimensional textile formwork.

These measures establish a "three-line defence": bolts and mesh form the first layer of support around the entry perimeter; roof cables provide the second layer by reinforcing the immediate roof; and the concrete backfill wall supplies a rigid third barrier that isolates the goaf. Field operation shows this composite system has ample bearing capacity, effectively transmits mining-induced loads, and prevents large-scale roof collapse. Monitoring data reveal virtually no damage to bolts, cables, or the backfill wall, confirming that the anchor–mesh–cable arrangement greatly enhances the stability of the retained entry.

6.3. Monitoring and Analysis of Surrounding-Rock Deformation

During retreat, an array of instruments was installed along the retained entry to record roadway convergence, roof-cable load, and wall pressure in real time. The data (Figures 24–26) reveal a staged deformation pattern. When the face lay 20–50 m from an instrument station, deformation accelerated; additional roof-to-floor convergence in this zone accounted for roughly half of the total closure. As the face advanced to within 50–100 m, convergence continued to rise—floor heave in particular increased rapidly from 75 mm to 160 mm. The cumulative closure reached about 340 mm, of which floor uplift contributed ≈65% (Figure 24). Both ribs bowed inward by roughly 60 mm, whereas roof subsidence remained comparatively small, underscoring that floor heave is the principal factor governing roadway stability.

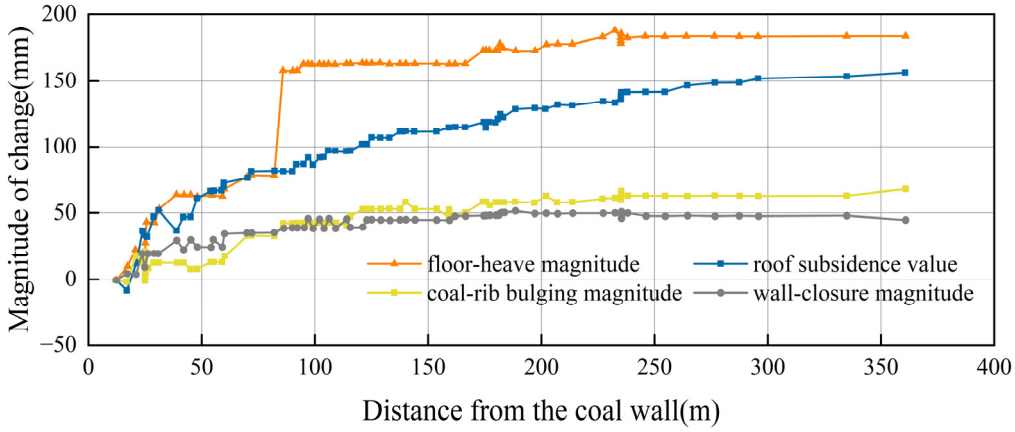

Figure 24. Convergence history of the retained entry.

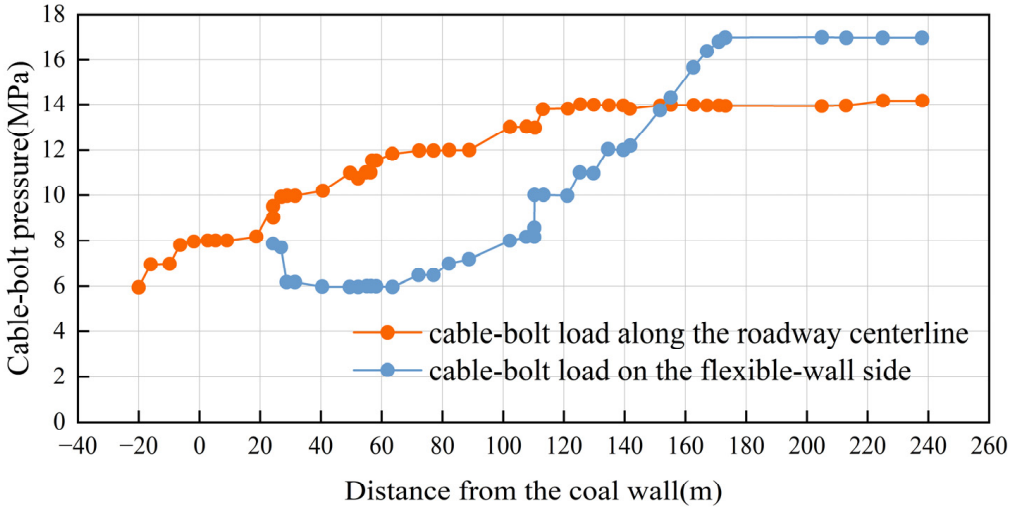

Figure 25. Evolution of roof-cable load at the flexible-formwork wall.

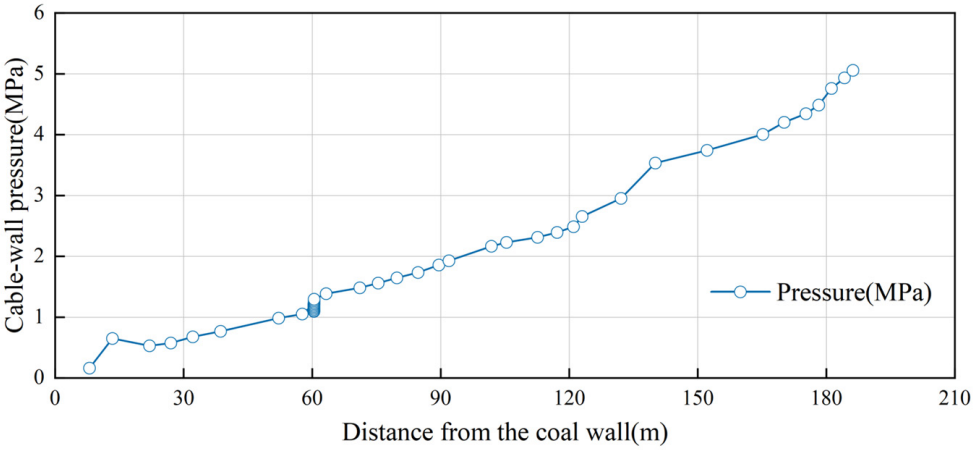

Figure 26. Pressure history of the flexible-formwork concrete wall.

Roof-cable loads evolved with mining (Figure 25). Along the roadway centre-line they rose gradually from 6 MPa at 20 m ahead of the face to 14 MPa at 120 m behind, then levelled off. On the gob-side, cable load jumped to a peak of 17 MPa at a 120 m lag before stabilising, indicating that release of early deformation increases cable demand—especially where the overhanging roof beam effect is strongest. Wall-pressure monitoring (Figure 26) shows that after casting, pressure climbed rapidly to an initial peak of 0.65 MPa at 25 m lag,

fell slightly to 0.53 MPa as the roof first fractured, and then rose again to about 5.05 MPa between 40 m and 200 m lag, corresponding to the first strong dynamic loading of the face. These observations confirm that the concrete wall carries most of the roof load at critical moments, while the adjacent cables delay deformation of the surrounding rock.

Overall, field monitoring verifies the effectiveness of the support design: the roadway remained within controllable limits and no support failures occurred. Deformation values and support loads stayed within acceptable ranges, demonstrating that the composite support system, combined with pre-splitting, effectively mitigates mining-induced impacts and ensures the long-term stability of the gob-side entry. Additionally, all recorded support loads remained within allowable limits. For example, the flexible concrete wall's peak pressure of 5.05 MPa was well below its compressive capacity, and the maximum cable load of 17 MPa remained under the yield threshold, providing quantitative confirmation that the support system had sufficient capacity in line with theoretical and simulation predictions.

6.4. Performance Assessment

To rigorously evaluate the effectiveness of the proposed three-line defence system, a comparison was performed between numerical simulation results and actual field monitoring data. Numerical analyses indicated significant reductions in roadway stress and deformation when utilising the combined approach. Specifically, the simulations showed that omitting the concrete backfill wall resulted in peak vertical stresses in the coal rib of approximately 22.4 MPa. In contrast, incorporating the backfill wall reduced this peak to around 13.1 MPa. Field monitoring further corroborated these findings, recording roadway convergence of approximately 340 mm, substantially less than the >500 mm typically observed with conventional supports in deep coal mining conditions [28]. The results indicate that this integrated support scheme suppresses roadway convergence by more than 30% compared with conventional techniques. Numerical results combined with field data indicate that the concrete backfill wall effectively absorbs residual stress from adjacent mined-out areas, thereby maintaining roadway stability. Consequently, each element of the three-line defence functions synergistically, significantly outperforming single-component support strategies in controlling roadway stability.

Furthermore, the proposed approach also exhibits clear advantages in cost-effectiveness, performance, and construction efficiency compared to traditional support methods such as high-water materials or U-shaped steel arches. Economically, flexible-formwork concrete walls, primarily utilising industrial waste such as coal gangue, have a unit cost of approximately ¥11,825 per linear metre (as detailed in Table 8). This figure is significantly lower than traditional pillar-retention methods. In terms of material expenses, using waste gangue as aggregate in the concrete mix reduces the cost by nearly 50% compared to proprietary high-water filling materials, making the solution more economical. In terms of structural performance, flexible-formwork concrete provides robust residual strength and substantial deformation capacity under high-pressure conditions, thereby offering reliable initial support and long-term stability. In contrast, a conventional narrow coal pillar or an unsupported gob-side typically cannot sustain high-pressure conditions and would result in larger deformation. The internal bolt-mesh-cable support ensured that the immediate roof and coal ribs remained intact, unlike traditional wooden or U-steel supports, which might buckle or lose effectiveness as the roof deforms. Constructability is also improved. The flexible formwork concrete approach allows rapid installation by pumping concrete and using a collapsible formwork bag, enabling construction to keep pace with face advancement. This mechanised process is safer and faster than manually erecting U-shaped steel supports or building pack walls, and it forms a continuous, sealed structure that enhances ventilation and fire prevention.

Table 8. Unit costs for gob-side entry retaining.

No.	Project Category	Description	Unit	Quantity	Unit Price (CNY)	Cost (CNY)
1	Filling body cost	Flexible-formwork concrete filling bag for coal mines	m^3	5.25	360	1890
2		C40 flexible-formwork concrete	m^3	4.8	800	3840
3		Rock bolts	set	5	50	250
4		Reinforcing ladder beam (rebar)	piece	4	50	200
5	Additional support cost	Rhomboid metal mesh	m^2	14	30	420
6		Cable bolts for goaf reinforcement	set	2	300	600
7	Roof cutting and pressure relief	Drilling and blasting	hole	1.2	1000	1200
8	Labour cost	Gob-side entry retaining crew	work-shift	15 work-shifts/2.4 m	500	3125
9	Roadway remediation	Rib trimming and floor cleaning	work-shift	9/15 m	500	300
Total		Unit cost per linear metre of gob-side entry retaining				11,825

Overall, compared to existing techniques, the proposed method offers a more cost-effective, higher-performance, and more easily implementable solution for gob-side entry retention in deep mines.

7. Conclusions

(1) Based on the geological conditions of the No. 3 seam at Xiadian Mine, the limit-equilibrium method and surrounding-rock stability analysis indicate that a minimum gob-side coal-pillar width of approximately 6 m is required, thereby providing a theoretical basis for pillar design.

(2) A pumpable C40 concrete mix for flexible formwork was developed by optimising its proportions and verifying strength. Tests at 28 days show that the compressive strength meets the design specification, providing reliable supplementary support for the retained entry.

(3) A three-dimensional FLAC3D model was established to evaluate stress distribution around the roadway for different pillar widths. The simulations show that increasing pillar width reduces stress concentration and enlarges the elastic core, thus enhancing roadway stability.

(4) A field programme combining deep-hole directional presplitting with a bolt–mesh–cable–concrete-wall composite support system was implemented at Panel 3118. Presplitting created a continuous fracture band in the hard roof, effectively relieving stress, while the composite support provided a "three-line defence" markedly improving surrounding-rock stability and preventing roof collapse.

While the proposed gob-side entry retaining technique has proven effective, ongoing monitoring is essential for assessing its long-term stability and adaptability to different geological conditions. Future research should focus on systematic comparisons with traditional methods, refinement of presplitting blast parameters for diverse roof conditions, and development of advanced numerical models. Additionally, numerical analyses should incorporate model calibration, sensitivity analysis, and mesh-independence checks to enhance simulation reliability.

Author Contributions: Conceptualization, C.M. and Y.Z.; methodology, C.M.; investigation, C.M., Y.P. and F.Z.; writing—original draft preparation, C.M.; writing—review and editing, Y.P., Y.Z. and F.Z. All authors have read and agreed to the published version of the manuscript.

Funding: This study was financially supported by the Key Research and Development of Xinjiang Uygur Autonomous Region, China (2023B01010).

Data Availability Statement: The raw data supporting the conclusions of this article will be made available by the authors on request.

Acknowledgments: The authors would like to express their thanks to technical staff for their efforts in preparation and testing of the specimens presented in this research.

Conflicts of Interest: Author Changle Ma was employed by the company Shanxi Lu'an Mining (Group) Co., Ltd. Author Yuewen Pan was employed by the company Xuchen Mining Technology Development (Xuzhou) Co., Ltd. Author Feng Zhou was employed by the company Wangzhuang Coal Industry Co., Ltd. Author Yafei Zhou was employed by the company Korla Jinchuan Mining Co., Ltd. The authors declare no conflicts of interest.

References

1. Yuan, L. Control of coal and gas outbursts in Huainan mines in China: A review. *J. Nat. Gas Sci. Eng.* **2016**, *33*, 38–57. [CrossRef]
2. Xie, S.R.; Wang, E.; Chen, D.; Li, H.; Jiang, Z.; Yang, H. Stability analysis and control technology of gob-side entry retaining with double roadways by filling with high-water material in gently inclined coal seam. *Int. J. Min. Sci. Technol.* **2022**, *32*, 112–125. [CrossRef]
3. Zhu, H.Z.; Wen, Z.-J.; Xu, L.; He, F.-L. Key technology of gob-side entry retained by roof cutting without coal pillar for hard main roof: A case study. *J. Cent. South Univ.* **2024**, *30*, 4097–4121. [CrossRef]
4. Hao, J.; Zhang, P.; Song, Y.; Liu, H.; Shi, Y.; Liu, J.; Lu, G. Research on Pillarless Mining by Gob-Side Caving under Soft Rock Roof Conditions: A Case Study. *Appl. Sci.* **2023**, *13*, 2816. [CrossRef]
5. Deng, Y.H.; Wang, S.Q. Feasibility analysis of gob-side entry retaining on a working face in a steep coal seam. *Int. J. Min. Sci. Technol.* **2014**, *24*, 499–503. [CrossRef]
6. Zhang, L.; Zhao, J.; Zang, C.; Wang, S. An innovative approach for gob-side entry retaining by roof cutting in steeply pitching seam longwall mining with hard roof: A case study. *Min. Metall. Explor.* **2020**, *37*, 1079–1091. [CrossRef]
7. Tian, X.; Wang, J.; Yu, G.; Wang, H.; Liu, P.; Pan, Z.; Wang, Y. Research and application of gob-side entry retaining with roof presplitting under residual coal pillar of upper coal seam. *Energy Explor. Exploit.* **2022**, *40*, 1494–1521. [CrossRef]
8. Shen, H.; Chen, Z.; Yuan, Y.; Li, B.; Anamor, S.K. Non-pillar coal mining by driving roadway during mining period in high-gas top-coal-caving working face. *Processes* **2024**, *12*, 2607. [CrossRef]
9. Lu, P.; Li, P.; Chen, J.; Zhang, C.; Xue, J.; Yu, T. Gas drainage from different mine areas: Optimal placement of drainage systems for deep coal seams with high gas emissions. *Int. J. Coal Sci. Technol.* **2015**, *2*, 84–90. [CrossRef]
10. Chen, X.; Feng, S.; Wang, L.; Jia, Q. Distribution and prevention of CO in a goaf of a working face with Y-type ventilation. *ACS Omega* **2021**, *6*, 1787–1796. [CrossRef]
11. Li, H.; Zu, H.; Zhang, K.; Qian, J. Study on filling support design and ground-pressure monitoring scheme for gob-side entry retention by roof cutting and pressure relief in high-gas thin coal seam. *Int. J. Environ. Res. Public Health* **2022**, *19*, 3913. [CrossRef]
12. Zhou, N.; Zhang, J.; Yan, H.; Li, M. Deformation behavior of hard roofs in solid backfill coal mining using physical models. *Energies* **2017**, *10*, 557. [CrossRef]
13. Zhang, N.; Han, C.L.; Kan, J.G.; Zheng, X.G. Surrounding-rock control theory and practice for gob-side entry retaining. *J. China Coal Soc.* **2014**, *39*, 1635–1641. (In Chinese)
14. Hua, X.Z.; Lu, X.Y.; Li, Y.F. Prevention and control technology of floor heave in gob-side entry retaining with large section of deep mine. *Coal Sci. Technol.* **2013**, *100–104.* (In Chinese)
15. Wu, G.; Chen, W.; Jia, S.; Tan, X.; Zheng, P.; Tian, H.; Rong, C. Deformation characteristics of a roadway in steeply inclined formations and its improved support. *Int. J. Rock Mech. Min. Sci.* **2020**, *130*, 104324. [CrossRef]
16. Zhang, Z.; Deng, M.; Bai, J.; Yan, S.; Yu, X. Stability control of gob-side entry retained under the gob with close-distance coal seams. *Int. J. Min. Sci. Technol.* **2021**, *31*, 321–332. [CrossRef]
17. Zhang, F.; Wang, X.; Bai, J.; Wang, G.; Wu, B. Post-peak mechanical characteristics of the high-water material for backfilling the gob-side entry retaining: From experiment to field application. *Arab. J. Geosci.* **2020**, *13*, 386. [CrossRef]
18. Wu, P.; Chen, L.; Li, M.; Wang, L.; Wang, X.; Zhang, W. Surrounding-rock stability control technology of roadway in large-inclination seam with weak structural plane in roof. *Minerals* **2021**, *11*, 881. [CrossRef]

19. Hua, X.Z.; Li, Y.F. Mechanics analysis on floor deformation of gob-side entry retaining and prevention and control of floor heave. *J. China Coal Soc.* **2016**, *41*, 1624–1631.
20. Huang, X.; Zhang, C.; Wang, Y.; He, J. Failure Analysis of Flexible Formwork Concrete Wall in Gob-Side Entry and Its Control Measures with Roof Cutting Technology. *J. Geophys. Eng.* **2025**, *22*, 909–923. [CrossRef]
21. Wang, H.; Guo, J. Research on the Deformation and Failure Mechanism of Flexible Formwork Walls in Gob-Side-Entry Retaining of Ultra-Long Isolated Mining Faces and Pressure Relief-Control Technology via Roof Cutting. *Appl. Sci.* **2025**, *15*, 5833. [CrossRef]
22. Li, W.; Bai, J.; Cheng, J.; Peng, S.; Liu, H. Determination of Coal-Rock Interface Strength by Laboratory Direct Shear Tests under Constant Normal Load. *Int. J. Rock Mech. Min. Sci.* **2015**, *77*, 60–67. [CrossRef]
23. Jiang, T.; Zhu, C.; Qiao, Y.; Sasaoka, T.; Shimada, H.; Hamanaka, A.; Li, W.; Chen, B. Deterioration Evolution Mechanism and Damage Constitutive Model Improvement of Sandstone–Coal Composite Samples under the Effect of Repeated Immersion. *Phys. Fluids* **2024**, *36*, 056611. [CrossRef]
24. Chen, S.; Jiang, T.; Wang, H.; Feng, F.; Yin, D.; Li, X. Influence of Cyclic Wetting-Drying on the Mechanical Strength Characteristics of Coal Samples: A Laboratory-Scale Study. *Energy Sci. Eng.* **2019**, *7*, 3020–3037. [CrossRef]
25. Xiong, Y.; Kong, D.; Cheng, Z.; Wen, Z.; Ma, Z.; Wu, G.; Liu, Y. Instability Control of Roadway Surrounding Rock in Close-Distance Coal Seam Groups under Repeated Mining. *Energies* **2021**, *14*, 5193. [CrossRef]
26. Jiang, T.; Cao, X.; Duan, H.; Shu, K. Recycling Efficiency Mechanism of Recycled Concrete Aggregate to Improve the CO_2 Uptake and Anti-Leakage Properties of CO_2 Sequestration Functional Backfills. *Constr. Build. Mater.* **2025**, *458*, 139663. [CrossRef]
27. Jiang, T.; Chen, B.; Bai, J.; Liu, B.; Chen, M. Improving Mechanism for Recycling Efficiency of Ceramic Construction Solid Waste and Properties of Composite Backfill Based on Aggregate Particle Size Distribution. *Constr. Build. Mater.* **2024**, *436*, 136826. [CrossRef]
28. Jia, M.; Bai, J.; Tian, T.; Xu, Y.; Qiu, L. Research on Pier Column Gob-Side Entry Retaining Technology. *Coal Sci. Technol.* **2014**, *42*, 18–22.